

1

2 The ANTsX Ecosystem for Mapping the 3 Mouse Brain

4 Nicholas J. Tustison¹, Min Chen², Fae N. Kronman³, Jeffrey T. Duda², Clare Gamlin⁴, Mia
5 G. Tustison, Michael Kunst⁴, Rachel Dalley⁴, Staci Sorenson⁴, Quanxi Wang⁴, Lydia Ng⁴,
6 Yongsoo Kim³, and James C. Gee²

7 ¹Department of Radiology and Medical Imaging, University of Virginia, Charlottesville, VA

8 ²Department of Radiology, University of Pennsylvania, Philadelphia, PA

9 ³Department of Neural and Behavioral Sciences, Penn State University, Hershey, PA

10 ⁴Allen Institute for Brain Science, Seattle, WA

11 _____

12 Corresponding authors:

13

14 Nicholas J. Tustison, DSc

15 Department of Radiology and Medical Imaging

16 University of Virginia

17 ntustison@virginia.edu

18

19 James C. Gee, PhD

20 Department of Radiology

21 University of Pennsylvania

22 gee@upenn.edu

²³ **Abstract**

²⁴ Precision mapping techniques coupled with high resolution image acquisition of the mouse
²⁵ brain permit the study of the spatial organization of gene activity and their mutual interaction
²⁶ for a comprehensive view of salient structural/functional relationships. Such research
²⁷ is facilitated by standardized anatomical coordinate systems, such as the well-known Allen
²⁸ Common Coordinate Framework (AllenCCFv3), and the ability to spatially map to such
²⁹ standardized spaces. The Advanced Normalization Tools Ecosystem is a comprehensive
³⁰ open-source software toolkit for generalized quantitative imaging with applicability to multiple
³¹ organ systems, modalities, and animal species. Herein, we illustrate the utility of
³² ANTsX for generating precision spatial mappings of the mouse brain and potential subsequent
³³ quantitation. We describe ANTsX-based workflows for mapping domain-specific image data to AllenCCFv3 accounting for common artefacts and other confounds. Novel
³⁴ contributions include ANTsX functionality for velocity flow-based mapping spanning the
³⁵ spatiotemporal domain of a longitudinal trajectory which we apply to the Developmental
³⁶ Common Coordinate Framework. Additionally, we present an automated structural morphological
³⁷ pipeline for determining volumetric and cortical thickness measurements analogous to the well-utilized ANTsX pipeline for human neuroanatomical structural morphology which
³⁸ illustrates a general open-source framework for tailored brain parcellations.

41 1 Introduction

42 Over the past two decades there have been significant advancements in mesoscopic analysis
43 of the mouse brain. It is currently possible to track single cell neurons in mouse brains,¹
44 observe whole brain developmental changes on a cellular level,² associate brain regions and
45 tissues with their genetic composition,³ and locally characterize neural connectivity.⁴ Much
46 of this scientific achievement has been made possible due to breakthroughs in high resolution
47 imaging techniques that permit submicron, 3-D imaging of whole mouse brains. Associated
48 research techniques such as micro-optical sectioning tomography,⁶ tissue clearing,^{1,7} spatial
49 transcriptomics⁹ are all well-utilized in the course of scientific investigations of mesoscale
50 relationships in the mouse brain.

51 An important component of this research is the ability to map the various image data to
52 anatomical reference frames¹¹ for inferring spatial relationships between structures, cells,
53 and genetics. This has motivated the development of detailed structural image atlases of
54 the mouse brain. Notable examples include the Allen Brain Atlas and Common Coordinate
55 Frameworks (AllenCCFv3),¹³ the Waxholm Space,¹⁴ and more recently, the Developmental
56 Common Coordinate Framework (DevCCF).¹⁵ Despite the significance of these contribu-
57 tions, challenges still exist in large part due to the wide heterogeneity in associated study-
58 specific image data. For example, variance in the acquisition methods can introduce artifacts
59 such as tissue distortion, holes, bubbles, folding, tears, and missing slices. These complicate
60 assumed correspondence for conventional spatial mapping approaches.

61 1.1 Mouse-specific brain mapping software

62 To address such challenges, several software packages have been developed over the years
63 comprising solutions of varying comprehensibility, sophistication, and availability. An
64 early contribution to the community was the Rapid Automatic Tissue Segmentation
65 (RATS) package¹⁶ for brain extraction. More recently, several publicly available packages
66 comprise well-established package dependencies originally developed on human brain data.
67 SPMMouse,¹⁷ for example, is based on the well-known Statistical Parametric Mapping

68 (SPM) Matlab-based toolset.¹⁸ The automated mouse atlas propagation (aMAP) tool is
69 largely a front-end for the NiftyReg image registration package¹⁹ applied to mouse data
70 which is currently available as a Python module.²⁰ NiftyReg is also used by the Atlas-based
71 Imaging Data Analysis (AIDA) MRI pipeline²¹ as well as the Multi Atlas Segmentation
72 and Morphometric Analysis Toolkit (MASMAT). Whereas the former also incorporates the
73 FMRIB Software Library (FSL)²² for brain extraction and DSISTudio²³ for DTI processing,
74 the latter uses NiftySeg and multi-consensus labeling tools²⁴ for brain extraction and
75 parcellation. In addition, MASMAT incorporates N4 bias field correction²⁵ from the
76 Advanced Normalization Tools Ecosystem (ANTsX)²⁶ as do the packages Multi-modal
77 Image Registration And Connectivity anaLysis (MIRACL),²⁷ Saammba-MRI,²⁸ and Small
78 Animal Magnetic Resonance Imaging (SAMRI).²⁹ However, whereas Saammba-MRI uses
79 AFNI³⁰ for image registration; MIRACL, SAMRI, SAMBA,³¹ and BrainsMapi³² all use
80 ANTsX registration tools. Other packages use landmark-based approaches to image regis-
81 tration including SMART—³³an R package for semi-automated landmark-based registration
82 and segmentation of mouse brain based on WholeBrain.³⁴ FriendlyClearMap³⁵ uses the
83 landmark-based registration functionality of Elastix.³⁶ Finally, the widespread adoption
84 of deep learning techniques has also influenced development in mouse brain imaging
85 methodologies. For example, if tissue deformations are not considered problematic for a
86 particular dataset, DeepSlice can be used to determine affine mappings³⁷ with the optimal
87 computational efficiency associated with neural networks.

88 1.2 The ANTsX Ecosystem for mouse brain mapping

89 As noted previously, many of the existing packages designed for processing mouse brain image
90 data use ANTsX tools for core processing steps in various workflows, particularly its pair-
91 wise, intensity-based image registration capabilities and bias field correction. Historically,
92 ANTsX development is originally based on fundamental approaches to image mapping,^{38–40}
93 particularly in the human brain, which has resulted in core contributions to the field such as
94 the well-known Symmetric Normalization (SyN) algorithm.⁴¹ Since its development, various
95 independent platforms have been used to evaluate ANTsX image registration capabilities

Table 1: Sampling of ANTsX functionality

<i>ANTsPy: Preprocessing</i>	
bias field correction	<code>n4_bias_field_correction(...)</code>
image denoising	<code>denoise_image(...)</code>
<i>ANTsPy: Registration</i>	
image registration	<code>registration(...)</code>
image transformation	<code>apply_transforms(...)</code>
template generation	<code>build_template(...)</code>
landmark registration	<code>fit_transform_to_paired_points(...)</code>
time-varying landmark reg.	<code>fit_time_varying_transform_to_point_sets(...)</code>
integrate velocity field	<code>integrate_velocity_field(...)</code>
invert displacement field	<code>invert_displacement_field(...)</code>
<i>ANTsPy: Segmentation</i>	
MRF-based segmentation	<code>atropos(...)</code>
Joint label fusion	<code>joint_label_fusion(...)</code>
diffeomorphic thickness	<code>kelly_kapowski(...)</code>
<i>ANTsPy: Miscellaneous</i>	
Regional intensity statistics	<code>label_stats(...)</code>
Regional shape measures	<code>label_geometry_measures(...)</code>
B-spline approximation	<code>fit_bspline_object_to_scattered_data(...)</code>
Visualize images and overlays	<code>plot(...)</code>
<i>ANTsPyNet: Mouse-specific</i>	
brain extraction	<code>mouse_brain_extraction(...modality="t2"...)</code> <code>mouse_brain_extraction(...modality="ex5"...)</code>
brain parcellation	<code>mouse_brain_parcellation(...)</code>
cortical thickness	<code>mouse_cortical_thickness(...)</code>
super resolution	<code>mouse_histology_super_resolution(...)</code>

ANTsX provides state-of-the-art functionality for processing biomedical image data. Such tools, including deep learning networks, support a variety of mapping-related tasks. A more comprehensive listing of ANTsX tools with self-contained R and Python examples is provided as a gist page on GitHub (<https://tinyurl.com/antsxtutorial>).

⁹⁶ in the context of different application foci which include multi-site brain MRI data,⁴² pul-
⁹⁷ monary CT data,⁴³ and most recently, multi-modal brain registration in the presence of
⁹⁸ tumors.⁴⁴

⁹⁹ Apart from its registration capabilities, ANTsX comprises additional functionality such
¹⁰⁰ as template generation,⁴⁵ intensity-based segmentation,⁴⁶ preprocessing,^{25,47} deep learning
¹⁰¹ networks,²⁶ and other miscellaneous utilities (see Table 1). The comprehensive use of the
¹⁰² toolkit has demonstrated superb performance in multiple application areas (e.g., consensus
¹⁰³ labeling,⁴⁸ brain tumor segmentation,⁴⁹ and cardiac motion estimation⁵⁰). Importantly,
¹⁰⁴ ANTs is built on the Insight Toolkit (ITK)⁵¹ deriving benefit from the open-source commu-
¹⁰⁵ nity of scientists and programmers as well as providing an important resource for algorith-
¹⁰⁶ mic development, evaluation, and improvement. We use this functionality to demonstrate
¹⁰⁷ recently developed frameworks for mapping fluorescence micro-optical sectioning tomogra-
¹⁰⁸ phy (fMOST) and multiplexed error-robust fluorescence *in situ* hybridization (MERFISH)
¹⁰⁹ image data to the AllenCCFv3 atlas space. In addition to standard preprocessing steps (e.g.,
¹¹⁰ bias correction), additional considerations are accommodated within the ANTsX ecosystem,
¹¹¹ such as section reconstruction and landmark-based alignment with corresponding processing
¹¹² scripts available at <https://github.com/dontminchenit/CCFAlignmentToolkit>.

¹¹³ 1.3 ANTsX-based open-source contributions

¹¹⁴ Consistent with previous ANTsX development, the newly introduced capabilities introduced
¹¹⁵ below are available through ANTsX (specifically, via R and Python ANTsX packages), and
¹¹⁶ illustrated through self-contained examples in the ANTsX tutorial (<https://tinyurl.com/antsxtutorial>) with a dedicated GitHub repository specific to this work (<https://github.com/ntustison/ANTsXMouseBrainMapping>).

¹¹⁹ 1.3.1 The DevCCF velocity flow model

¹²⁰ Recently, the Developmental Common Coordinate Framework (DevCCF) was introduced to
¹²¹ the mouse brain research community as a public resource¹⁵ comprising symmetric atlases

122 of multimodal image data and anatomical segmentations defined by developmental ontol-
123 ogy. These templates sample the mouse embryonic days (E) 11.5, E13.5, E15.5, E18.5 and
124 postnatal day (P) 4, P14, and P56. Modalities include light sheet florescence microscopy
125 (LSFM) and at least four MRI contrasts per developmental stage. Anatomical parcellations
126 are also available for each time point and were generated from ANTsX-based mappings of
127 gene expression and other cell type data. Additionally, the P56 template was integrated
128 with the AllenCCFv3 to further enhance the practical utility of the DevCCF. These pro-
129 cesses, specifically template generation and multi-modal image mapping, were performed
130 using ANTsX functionality in the presence of image mapping difficulties such as missing
131 data and tissue distortion.¹⁵

132 Given the temporal gaps in the discrete set of developmental atlases, we also provide an
133 open-source framework for inferring correspondence within the temporally continuous do-
134 main sampled by the existing set of embryonic and postnatal atlases of the DevCCF. This
135 recently developed functionality permits the generation of a diffeomorphic velocity flow trans-
136 formation model,⁵² influenced by previous work.⁵³ The resulting time-parameterized velocity
137 field spans the stages of the DevCCF where mappings between any two continuous time
138 points within the span bounded by the E11.5 and P56 atlases is determined by integration
139 of the optimized velocity field.

140 1.3.2 Structural morphology and cortical thickness in the mouse brain

141 One of the most frequently utilized pipelines in the ANTsX toolkit is that of estimating corti-
142 cal thickness maps in the human brain. Beginning with the Diffeomorphic Registration-based
143 Cortical Thickness (DiReCT) algorithm,⁵⁴ this was later expanded to include a complete pro-
144 cessing framework for human brain cortical thickness estimation for both cross-sectional⁵⁵
145 and longitudinal⁵⁶ data using T1-weighted MRI. These pipelines were later significantly
146 refactored using deep learning innovations.²⁶

147 In contrast to the pipeline development in human data,²⁶ no current ANTsX tools exist to
148 create adequate training data for the mouse brain. In addition, mouse brain data acquisition
149 often has unique issues, such as lower data quality or sampling anisotropy which limits

150 its applicability to high resolution resources (e.g., AllenCCFv3, DevCCF), specifically with
151 respect to the corresponding granular brain parcellations derived from numerous hours of
152 expert annotation leveraging multimodal imaging resources.

153 Herein, we introduce a mouse brain cortical thickness pipeline for T2-weighted (T2-w) MRI
154 comprising two novel deep learning components: two-shot learning brain extraction from
155 data augmentation of two ANTsX templates generated from two open datasets^{57,58} and
156 single-shot brain parcellation derived from the AllenCCFv3 labelings mapped to the corre-
157 sponding DevCCF P56 T2-w component. Although we anticipate that this cortical thickness
158 pipeline will be beneficial to the research community, this work demonstrates more generally
159 how one can leverage ANTsX tools for developing tailored brain parcellation schemes using
160 these publicly available resources. Evaluation is performed on an independent open dataset⁵⁹
161 comprising longitudinal acquisitions of multiple specimens.

162 **2 Results**

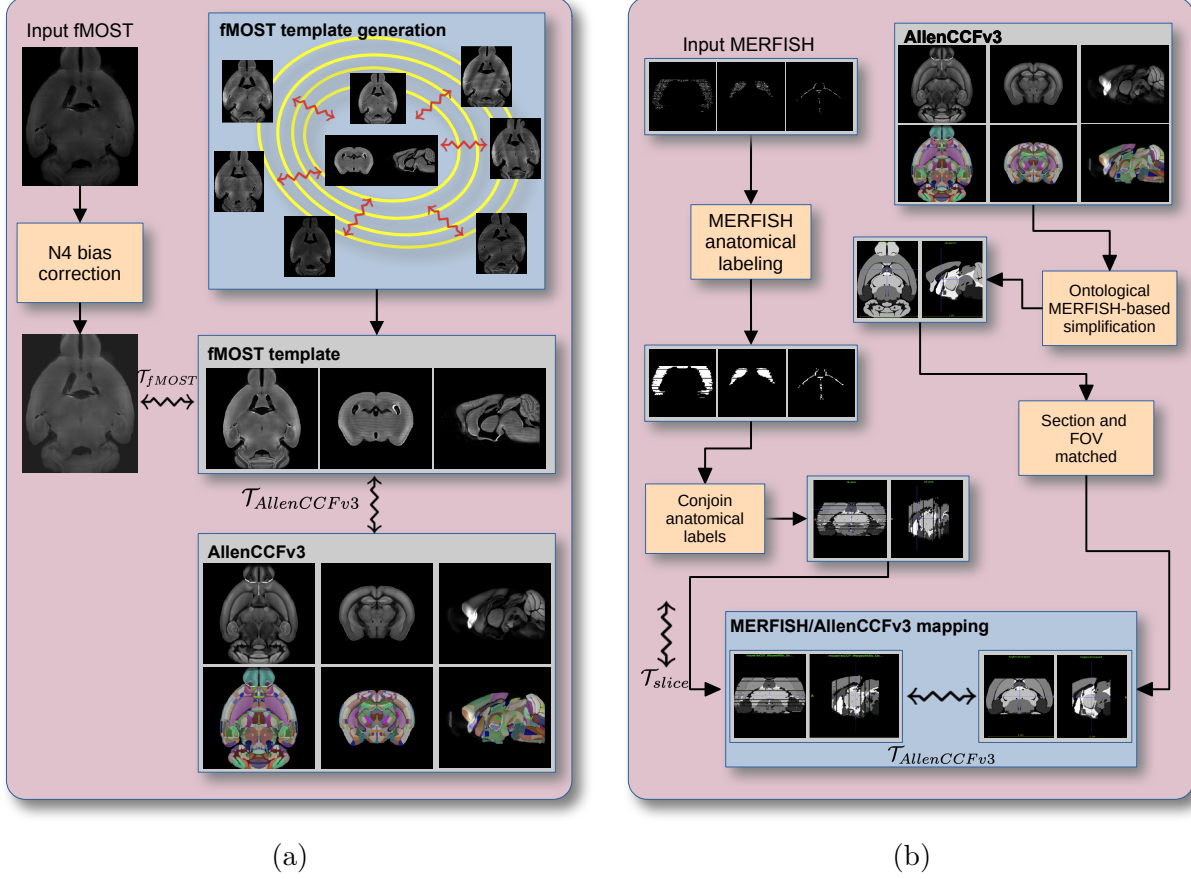


Figure 1: Diagrammatic illustration of the two ANTsX-based pipelines for mapping (a) fMOST and (b) MERFISH data into the space of AllenCCFv3. Each generates the requisite transforms, \mathcal{T} , to map individual images.

163 **2.1 AllenCCFv3 brain image mapping**

164 **2.1.1 Mapping fluorescence micro-optical sectioning tomography data**

165 **Overview.** A framework for mapping fluorescence micro-optical sectioning tomography
 166 (fMOST) mouse brain images into the AllenCCFv3 was developed (see Figure 1(a)). An
 167 intensity- and shape-based average fMOST atlas serves as an intermediate registration target
 168 for mapping fMOST images from individual specimens into the AllenCCFv3. Preprocess-
 169 ing steps include downsampling to match the $25\mu m$ isotropic AllenCCFv3, acquisition-based

stripe artifact removal, and inhomogeneity correction.²⁵ Preprocessing also includes a single annotation-driven registration to establish a canonical mapping between the fMOST atlas and the AllenCCFv3. This step allows us to align expert determined landmarks to accurately map structures with large morphological differences between the modalities, which are difficult to address using standard approaches. Once this canonical mapping is established, standard intensity-based registration is used to align each new fMOST image to the fMOST specific atlas. This mapping is concatenated with the canonical fMOST atlas-to-AllenCCFv3 mapping to further map each individual brain into the latter without the need to generate additional landmarks. Transformations learned through this mapping can be applied to single neuron reconstructions from the fMOST images to evaluate neuronal distributions across different specimens into the AllenCCFv3 for the purpose of cell census analyses.

Data. The high-throughput and high-resolution fluorescence micro-optical sectioning tomography (fMOST)^{60,61} platform was used to image 55 mouse brains containing gene-defined neuron populations, with sparse transgenic expression.^{62,63} In short, the fMOST imaging platform results in 3-D images with voxel sizes of $0.35 \times 0.35 \times 1.0\mu\text{m}^3$ and is a two-channel imaging system where the green channel displays the green fluorescent protein (GFP) labeled neuron morphology and the red channel is used to visualize the counterstained propidium iodide cytoarchitecture. The spatial normalizations described in this work were performed using the red channel, which offered higher tissue contrast for alignment, although other approaches are possible including multi-channel registration.

Evaluation. Evaluation of the canonical fMOST atlas to Allen CCFv3 mapping was performed via quantitative comparison at each step of the registration and qualitative assessment of structural correspondence after alignment by an expert anatomist. Dice values were generated for the following structures: whole brain, 0.99; fimbria, 0.91; habenular commissure, 0.63; posterior choroid plexus, 0.93; anterior choroid plexus, 0.96; optic chiasm, 0.77; caudate putamen, 0.97. Similar qualitative assessment was performed for each fMOST specimen including the corresponding neuron reconstruction data.

¹⁹⁷ **2.1.2 Mapping multiplexed error-robust fluorescence in situ hybridization**
¹⁹⁸ **(MERFISH) data**

¹⁹⁹ **Overview.** The unique aspects of mapping multiplexed error-robust fluorescence in situ
²⁰⁰ hybridization (MERFISH) spatial transcriptomic data onto AllenCCFv3⁶⁴ required the de-
²⁰¹velopment of a separate ANTsX-based pipeline (see Figure 1(b)). Mappings are performed
²⁰² by matching gene expression derived region labels from the MERFISH data to corresponding
²⁰³anatomical parcellations of the AllenCCFv3. The pipeline consists of MERFISH data spe-
²⁰⁴cific preprocessing which includes section reconstruction, mapping corresponding anatomical
²⁰⁵labels between AllenCCFv3 and the spatial transcriptomic maps of the MERFISH data, and
²⁰⁶matching MERFISH sections to the atlas space. Following pre-processing, two main align-
²⁰⁷ment steps were performed: 1) 3-D global affine mapping and section matching of the Al-
²⁰⁸lenCCFv3 into the MERFISH data and 2) 2D global and deformable mapping between each
²⁰⁹MERFISH section and matched AllenCCFv3 section. Mappings learned via each step in the
²¹⁰pipeline are preserved and concatenated to provide point-to-point correspondence between
²¹¹the original MERFISH data and AllenCCFv3, thus allowing individual gene expressions to
²¹²be transferred into the AllenCCFv3.

²¹³ **Data.** MERFISH mouse brain data was acquired using a previously detailed procedure.⁶⁴
²¹⁴ Briefly, a brain of C57BL/6 mouse was dissected according to standard procedures and
²¹⁵placed into an optimal cutting temperature (OCT) compound (Sakura FineTek 4583) in
²¹⁶which it was stored at -80°C. The fresh frozen brain was sectioned at 10 μm on Leica 3050
²¹⁷S cryostats at intervals of 200 μm to evenly cover the brain. A set of 500 genes were imaged
²¹⁸that had been carefully chosen to distinguish the ~ 5200 clusters of our existing RNAseq
²¹⁹taxonomy. For staining the tissue with MERFISH probes, a modified version of instructions
²²⁰provided by the manufacturer was used.⁶⁴ Raw MERSCOPE data were decoded using Vizgen
²²¹software (v231). Cell segmentation was performed.⁶⁵ In brief, cells were segmented based
²²²on DAPI and PolyT staining using Cellpose.⁶⁶ Segmentation was performed on a median
²²³z-plane (fourth out of seven) and cell borders were propagated to z-planes above and below.
²²⁴ To assign cluster identity to each cell in the MERFISH dataset, we mapped the MERFISH
²²⁵cells to the scRNA-seq reference taxonomy.

226 **Evaluation.** Alignment of the MERFISH data into the AllenCCFv3 was qualitatively as-
227 sessed by an expert anatomist at each iteration of the registration using known correspon-
228 dence of gene markers and their associations with the AllenCCFv3. As previously reported,⁶⁴
229 further assessment of the alignment showed that, of the 554 terminal regions (gray matter
230 only) in the AllenCCFv3, only seven small subregions were missed from the MERFISH
231 dataset: frontal pole, layer 1 (FRP1), FRP2/3, FRP5; accessory olfactory bulb, glomerular
232 layer (AOBgl); accessory olfactory bulb, granular layer (AOBgr); accessory olfactory bulb,
233 mitral layer (AOBmi); and accessory supraoptic group (ASO).

234 **2.2 The DevCCF velocity flow model**

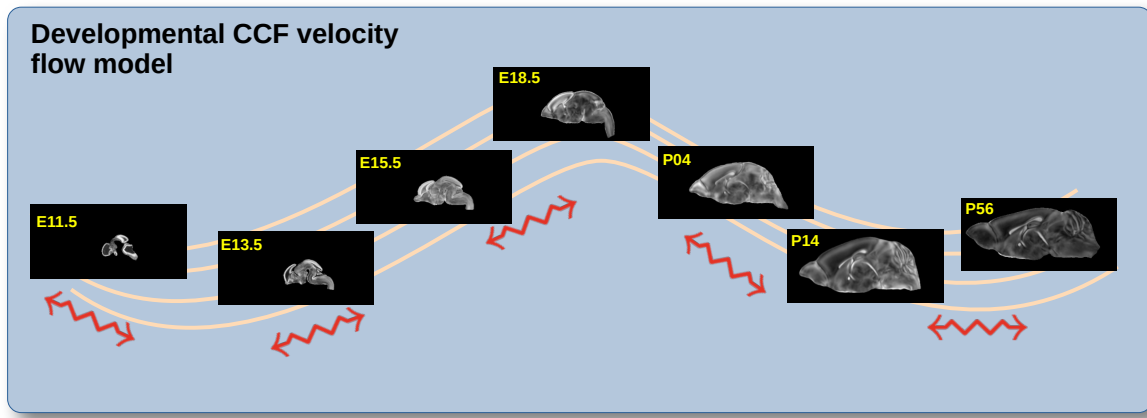


Figure 2: The spatial transformation between any two time points within the DevCCF longitudinal developmental trajectory is available through the use of ANTsX functionality for generating a velocity flow model.

235 To continuously interpolate transformations between the different stages of the DevCCF
236 atlases, a velocity flow model was constructed using DevCCF derived data and functionality
237 recently introduced into both the ANTsR and ANTsPy packages. Both platforms include
238 a complete suite of functions for determining dense correspondence from sparse landmarks
239 based on a variety of transformation models ranging from standard linear models (i.e., rigid,
240 affine) to deformable diffeomorphic models (e.g, symmetric normalization).⁴¹ The latter set
241 includes transformation models for both the pairwise scenario and for multiple sets, as in the

²⁴² case of the DevCCF. ANTsX, being built on top of ITK, uses an ITK image data structure
²⁴³ for the 4-D velocity field where each voxel contains the x , y , z components of the field at
²⁴⁴ that point.

²⁴⁵ **2.2.1 Data**

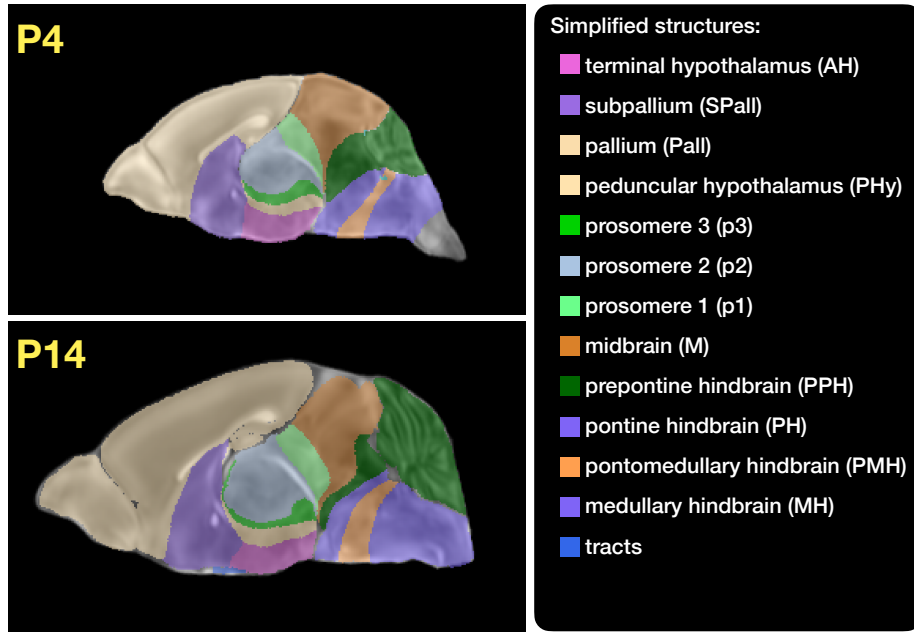


Figure 3: Annotated regions representing common labels across developmental stages which are illustrated for both P4 and P14.

²⁴⁶ Labeled annotations are available as part of the original DevCCF and reside in the space
²⁴⁷ of each developmental template which range in resolution from $31.5 - 50\mu\text{m}$. Across all
²⁴⁸ atlases, the total number of labeled regions exceeds 2500. From these labels, a common set
²⁴⁹ of 26 labels (13 per hemisphere) across all atlases were used for optimization and evaluation.

²⁵⁰ These simplified regions include: terminal hypothalamus, subpallium, pallium, peduncular
²⁵¹ hypothalamus, prosomere, prosomere, prosomere, midbrain, prepontine hindbrain, pontine
²⁵² hindbrain, pontomedullary hindbrain, medullary hindbrain, and tracts (see Figure 3).

²⁵³ Prior to velocity field optimization, all data were rigidly transformed to DevCCF P56 using
²⁵⁴ the centroids of the common label sets. In order to determine the landmark correspondence
²⁵⁵ across DevCCF stages, the multi-metric capabilities of `ants.registration(...)` were used.

256 Instead of performing intensity-based pairwise registration directly on these multi-label im-
 257 ages, each label was used to construct a separate fixed and moving image pair resulting in a
 258 multi-metric registration optimization scenario involving 24 binary image pairs (each label
 259 weighted equally) for optimizing diffeomorphic correspondence between neighboring time
 260 point atlases using the mean squares metric and the symmetric normalization transform.⁴¹
 261 To generate the set of common point sets across all seven developmental atlases, the label
 262 boundaries and whole regions were sampled in the P56 atlas and then propagated to each
 263 atlas using the transformations derived from the pairwise registrations. We selected a sam-
 264 pling rate of 10% for the contour points and 1% for the regional points for a total number
 265 of points being per atlas being 173303 ($N_{contour} = 98151$ and $N_{region} = 75152$). Regional
 266 boundary points were weighted twice as those of non-boundary points during optimization.

267 2.2.2 Optimization

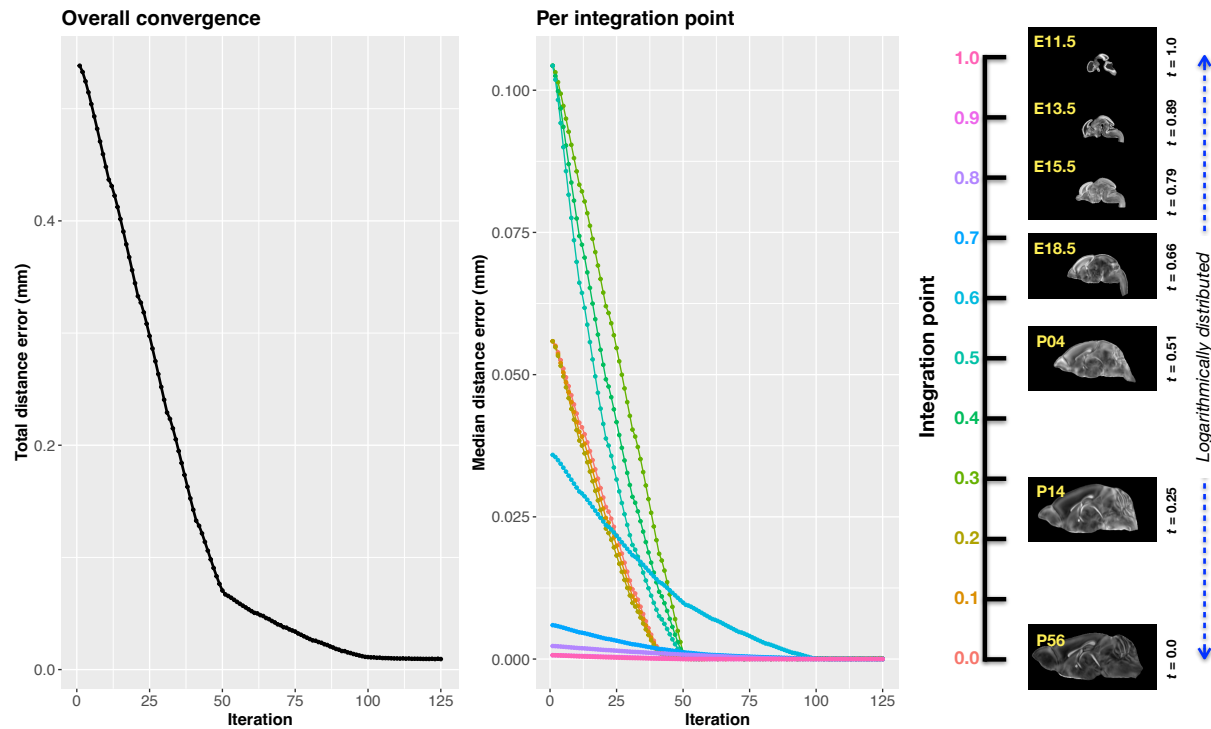


Figure 4: Convergence of the optimization of the velocity field for describing the transformation through the developmental stages from E11.5 through P56.

268 The velocity field was optimized using the input composed of the seven corresponding point

269 sets and their associated weight values, the selected number of integration points for the
270 velocity field ($N = 11$), and the parameters defining the geometry of the spatial dimensions
271 of the velocity field. Thus, the optimized velocity field described here is of size [256, 182, 360]
272 ($50\mu\text{m}$ isotropic) $\times 11$ integration points for a total compressed size of a little over 2 GB.
273 This choice represented weighing the trade-off between tractability, portability, and accuracy.
274 However, all data and code to reproduce the results described (with possible variation in the
275 input parameters) are available in the dedicated GitHub repository.

276 The normalized time point scalar value for each atlas/point-set in the temporal domains [0, 1]
277 was also defined. Given the increasingly larger gaps in the postnatal timepoint sampling, we
278 made two adjustments. Based on known mouse brain development, we used 28 days for the
279 P56 data. We then computed the log transform of the adjusted set of time points prior to
280 normalization between 0 and 1 (see the right side of Figure 4). This log transform, as part
281 of the temporal normalization, significantly improved data spacing.

282 The maximum number of iterations was set to 200 with each iteration taking approximately
283 six minutes on a 2020 iMac (processor, 3.6 GHz 10-Core Intel Core i9; memory, 64 GB 2667
284 MHz DDR4) At each iteration we looped over the 11 integration points. At each integration
285 point, the velocity field estimate was updated by warping the two immediately adjacent
286 point sets to the integration time point and determining the regularized displacement field
287 between the two warped point sets. As with any gradient-based descent algorithm, this field
288 was multiplied by a small step size ($\delta = 0.2$) before adding to the current velocity field.
289 Convergence is determined by the average displacement error over each of the integration
290 points. As can be seen in the left panel of Figure 4, convergence occurred around 125
291 iterations when the average displacement error over all integration points is minimized. The
292 median displacement error at each of the integration points also trends towards zero but at
293 different rates.

294 2.2.3 The transformation model

295 Once optimized, the resulting velocity field can be used to generate the deformable transform
296 between any two continuous points within the time interval bounded by E11.5 and P56. In

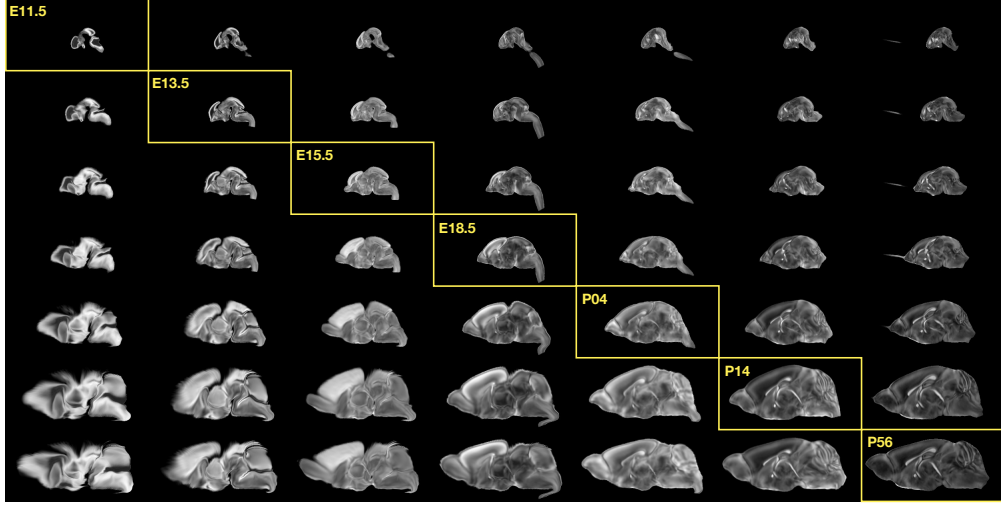


Figure 5: Mid-sagittal visualization of the effects of the transformation model in warping every developmental stage to the time point of every other developmental stage. The original images are located along the diagonal. Columns correspond to the warped original image whereas the rows represent the reference space to which each image is warped.

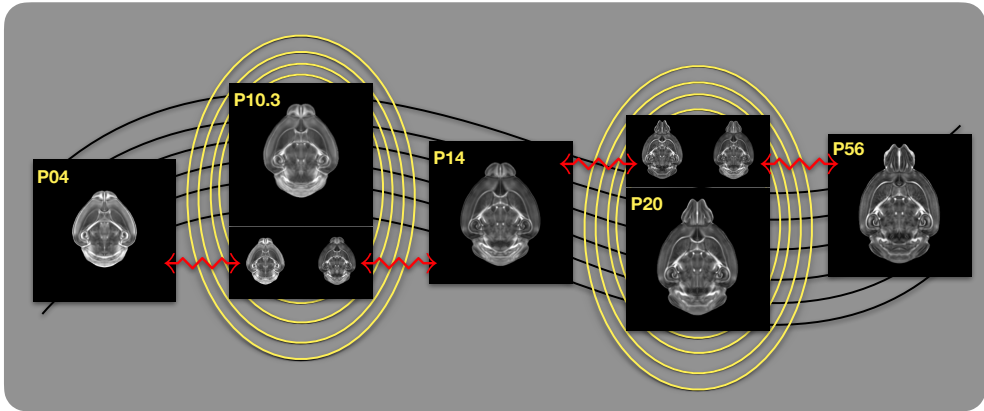


Figure 6: Illustration of the use of the velocity flow model for creating virtual templates at continuous time points not represented in one of the existing DevCCF time points. For example, FA templates at time point P10.3 and P20 can be generated by warping the existing temporally adjacent developmental templates to the target time point and using those images in the ANTsX template building process.

297 Figure 5, we transform each atlas to the space of every other atlas using the DevCCF
 298 transform model. Additionally, one can use this transformation model to construct virtual
 299 templates in the temporal gaps of the DevCCF. Given an arbitrarily chosen time point
 300 within the normalized time point interval, the existing adjacent DevCCF atlases on either
 301 chronological side can be warped to the desired time point. A subsequent call to one of

302 the ANTsX template building functions then permits the construction of the template at
 303 that time point. In Figure 6, we illustrate the use of the DevCCF velocity flow model for
 304 generating two such virtual templates for two arbitrary time points. Note that both of these
 305 usage examples can be found in the GitHub repository previously given.

306 2.3 The Mouse Cortical Thickness Pipeline

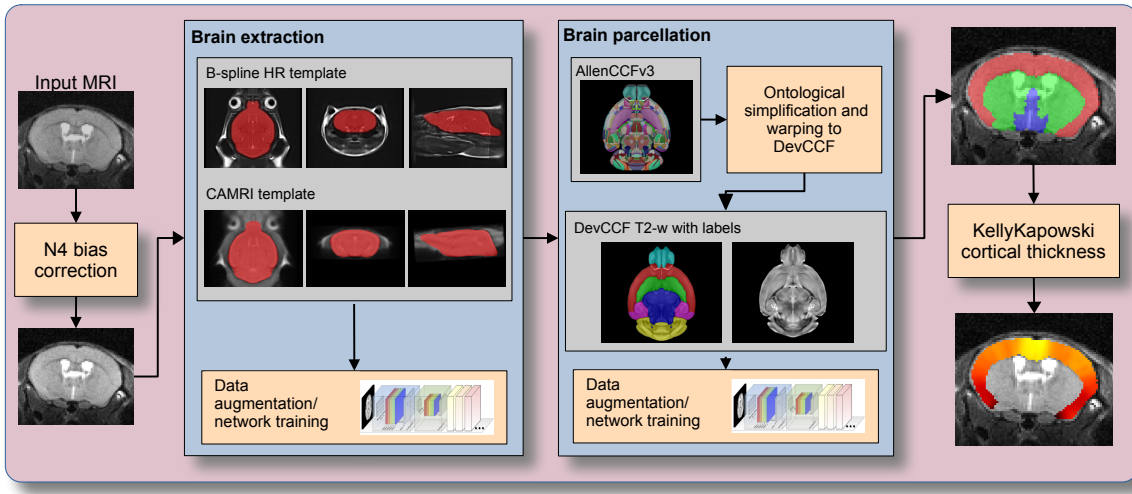


Figure 7: The mouse brain cortical thickness pipeline integrating two deep learning components for brain extraction and brain parcellation prior to estimating cortical thickness. Both deep learning networks rely heavily on data augmentation on templates built from open data and provide an outline for further refinement and creating alternative parcellations for tailored research objectives.

307 One of the most well-utilized pipelines in the ANTsX toolkit is the generation of corti-
 308 cal thickness maps in the human brain from T1-weighted MRI. Starting with the novel
 309 Diffeomorphic Registration-based Cortical Thickness (DiReCT) algorithm,⁵⁴ a complete al-
 310 gorithmic workflow was developed for both cross-sectional⁵⁵ and longitudinal⁵⁶ T1-weighted
 311 MR image data. This contribution was later refactored using deep learning²⁶ leveraging the
 312 earlier results⁵⁵ for training data.

313 In the case of the mouse brain, the lack of training data and/or tools to generate training
 314 data making analogous algorithmic development difficult. In addition, mouse data is often
 315 characterized by unique issues such as frequent anisotropic sampling which are often in sharp

316 contrast to the high resolution resources available within the community, e.g., AllenCCFv3
317 and DevCCF. Using ANTsX and other publicly available data resources, we developed a
318 complete mouse brain structural morphology pipeline as illustrated in Figure 7 and detailed
319 below.

320 2.3.1 Two-shot mouse brain extraction network

321 In order to create a generalized mouse brain extraction network, we built whole-head tem-
322 plates from two publicly available datasets. The Center for Animal MRI (CAMRI) dataset⁵⁷
323 from the University of North Carolina at Chapel Hill consists of 16 T2-weighted MRI volumes
324 of voxel resolution $0.16 \times 0.16 \times 0.16 mm^3$. The second high-resolution dataset⁵⁸ comprises
325 88 specimens each with three spatially aligned canonical views with in-plane resolution of
326 $0.08 \times 0.08 mm^2$ with a slice thickness of $0.5 mm$. These three orthogonal views were used to
327 reconstruct a single high-resolution volume per subject using a B-spline fitting algorithm de-
328 veloped in ANTsX.⁶⁷ From these two datasets, two symmetric isotropic ANTsX templates⁴⁵
329 were generated analogous to the publicly available ANTsX human brain templates used
330 in previous research.⁵⁵ Bias field simulation, intensity histogram warping, noise simulation,
331 random translation and warping, and random anisotropic resampling in the three canon-
332 ical directions were used for data augmentation in training a T2-weighted brain extraction
333 network.

334 2.3.2 Single-shot mouse brain parcellation network

335 To create the network for generating a brain parcellation consistent with cortical thickness
336 estimation, we used the AllenCCFv3 and the associated `allensdk` Python library. Using
337 `allensdk`, a gross parcellation labeling was generated from the fine Allen CCFv3 labeling
338 which includes the cerebral cortex, cerebral nuclei, brain stem, cerebellum, main olfactory
339 bulb, and hippocampal formation. This labeling was mapped to the P56 component of
340 the DevCCF. Both the T2-w P56 DevCCF and labelings, in conjunction with the data
341 augmentation described previously for brain extraction, was used to train a brain parcellation
342 network.

343 **2.3.3 Evaluation**

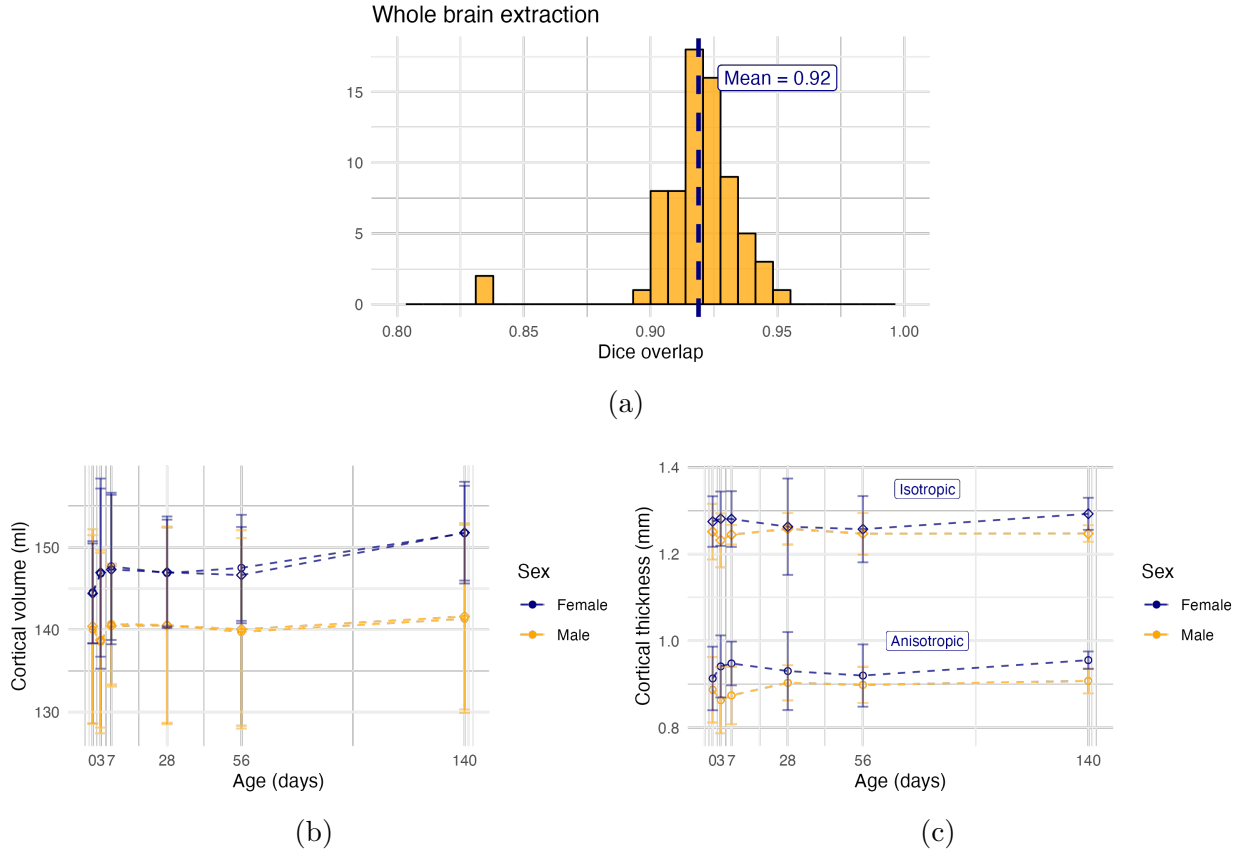


Figure 8: Evaluation of the ANTsX mouse brain extraction, parcellation, and cortical thickness pipeline on an independent dataset consisting of 12 specimens \times 7 time points = 84 total images. (a) Dice overlap comparisons with the provided brain masks provide generally good agreement with the brain extraction network. (b) Cortical volume measurements show similar average quantities over growth and development between the original anisotropic data and interpolated isotropic data. (c) These results contrast with the cortical thickness measurements which show that cortical thickness estimation in anisotropic space severely underestimates the actual values.

344 For evaluation, we used an additional publicly available dataset⁵⁹ which is completely in-
 345 dependent from the data used in training the brain extraction and parcellation networks.
 346 Data includes 12 specimens each imaged at seven time points (Day 0, Day 3, Week 1, Week
 347 4, Week 8, Week 20) with available brain masks. In-plane resolution is $0.1 \times 0.1 mm^2$ with
 348 a slice thickness of $0.5 mm$. Since the training data is isotropic and data augmentation in-
 349 cludes downsampling in the canonical directions, each of the two networks learns mouse
 350 brain-specific interpolation such that one can perform prediction on thick-sliced images, as,

³⁵¹ for example, in these evaluation data, and return isotropic probability and thickness maps (a
³⁵² choice available to the user). Figure 8 summarizes the results of the evaluation and compar-
³⁵³ ison between isotropic and anisotropic cortical measurements in male and female specimens.

354 **3 Discussion**

355 The ANTsX ecosystem is a powerful framework that has demonstrated applicability to mul-
356 tiple species and organ systems, including the mouse brain. This is further evidenced by the
357 many software packages that use various ANTsX components in their own mouse-specific
358 workflows. In and of itself, the extensive functionality of ANTsX makes it possible to create
359 complete processing pipelines without requiring the integration of multiple packages. These
360 open-source components not only perform well but are available across multiple platforms
361 which facilitates the construction of tailored pipelines for individual study solutions. These
362 components are also supported by years of development not only by the ANTsX development
363 team but by the larger ITK community.

364 In the case of the development of the DevCCF, ANTsX was crucial in providing necessary
365 functionality for yielding high quality output. For the generation of the individual develop-
366 mental stage multi-modal, symmetric templates, ANTsX is unique amongst image analysis
367 software packages in providing existing solutions for template generation which have been
368 thoroughly vetted, including being used in several studies over the years, and which continue
369 to be under active refinement. At its core, computationally efficient and quality template
370 generation requires the use of precision pairwise image mapping functionality which, histori-
371 cally, is at the origins of the ANTsX ecosystem. Moreover, these mapping capabilities extend
372 beyond template generation to the mapping of other image data (e.g., gene expression maps)
373 to a selected template for providing further insight into the mouse brain.

374 With respect to the DevCCF, despite the significant expansion of available developmental age
375 templates beyond what existed previously, there are still temporal gaps in the DevCCF which
376 can be potentially sampled by future research efforts. However, pioneering work involving
377 time-varying diffeomorphic transformations allow us to continuously situate the existing
378 templates within a velocity flow model. This allows one to determine the diffeomorphic
379 transformation from any one temporal location to any other temporal location within the
380 time span defined by the temporal limits of the DevCCF. This functionality is built on
381 multiple ITK components including the B-spline scattered data approximation technique for
382 field regularization and velocity field integration. This velocity field model permits intra-

³⁸³ template comparison and the construction of virtual templates where a template can be
³⁸⁴ estimated at any continuous time point within the temporal domain. This novel application
³⁸⁵ can potentially enhance our understanding of intermediate developmental stages.

³⁸⁶ We also presented a mouse brain pipeline for brain extraction, parcellation, and cortical
³⁸⁷ thickness using single-shot and two-shot learning with data augmentation. This approach
³⁸⁸ attempts to circumvent (or at least minimize) the typical requirement of large training
³⁸⁹ datasets as with the human ANTsX pipeline analog. However, even given our initial success
³⁹⁰ on independent data, we fully anticipate that refinements will be necessary. Given that the
³⁹¹ ANTsX toolkit is a dynamic effort undergoing continual improvement, we manually correct
³⁹² cases that fail and use them for future training and refinement of network weights as we have
³⁹³ done for our human-based networks. Generally, these approaches provide a way to bootstrap
³⁹⁴ training data for manual refinement and future generation of more accurate deep learning
³⁹⁵ networks in the absence of other applicable tools.

396 **4 Methods**

397 The following methods are all available as part of the ANTsX ecosystem with analogous
398 elements existing in both ANTsR (ANTs in R) and ANTsPy (ANTs in Python) with an
399 ANTs/ITK C++ core. However, most of the development for the work described below was
400 performed using ANTsPy. For equivalent calls in ANTsR, please see the ANTsX tutorial at
401 <https://tinyurl.com/antsxtutorial>.

402 **4.1 General ANTsX utilities**

403 **4.1.1 Preprocessing: bias field correction and denoising**

404 Bias field correction and image denoising are standard preprocessing steps in improving over-
405 all image quality in mouse brain images. The bias field, a gradual spatial intensity variation
406 in images, can arise from various sources such as magnetic field inhomogeneity or acquisition
407 artifacts, leading to distortions that can compromise the quality of brain images. Correct-
408 ing for bias fields ensures a more uniform and consistent representation of brain structures,
409 enabling more accurate quantitative analysis. Additionally, brain images are often suscep-
410 tible to various forms of noise, which can obscure subtle features and affect the precision
411 of measurements. Denoising techniques help mitigate the impact of noise, enhancing the
412 signal-to-noise ratio and improving the overall image quality. The well-known N4 bias field
413 correction algorithm²⁵ has its origins in the ANTs toolkit which was implemented and intro-
414 duced into the ITK toolkit, i.e. `ants.n4_bias_field_correction(...)`. Similarly, ANTsX
415 contains an implementation of a well-performing patch-based denoising technique⁴⁷ and is
416 also available as an image filter to the ITK community, `ants.denoise_image(...)`.

417 **4.1.2 Image registration**

418 The ANTs registration toolkit is a complex framework permitting highly tailored solu-
419 tions to pairwise image registration scenarios.⁶⁸ It includes innovative transformation mod-
420 els for biological modeling^{41,53} and has proven capable of excellent performance.^{42,69} Var-

421 ious parameter sets targeting specific applications have been packaged with the different
422 ANTsX packages, specifically ANTs, ANTsPy, and ANTsR.²⁶ In ANTsPy, the function
423 `ants.registration(...)` is used to register a pair of images or a pair of image sets where
424 `type_of_transform` is a user-specified option that invokes a specific parameter set. For ex-
425 ample `type_of_transform='antsRegistrationSyNQuick[s]`' encapsulates an oft-used pa-
426 rameter set for quick registration whereas `type_of_transform='antsRegistrationSyN[s]`'
427 is a more detailed alternative. Transforming images using the derived transforms is performed
428 via the `ants.apply_transforms(...)` function.

429 Initially, linear optimization is initialized with center of (intensity) mass alignment typically
430 followed by optimization of both rigid and affine transforms using the mutual information
431 similarity metric. This is followed by diffeomorphic deformable alignment using symmetric
432 normalization (SyN) with Gaussian⁴¹ or B-spline regularization⁵³ where the forward trans-
433 form is invertible and differentiable. The similarity metric employed at this latter stage is
434 typically either neighborhood cross-correlation or mutual information. Note that these pa-
435 rameter sets are robust to input image type (e.g., light sheet fluorescence microscopy, Nissl
436 staining, and the various MRI modalities) and are adaptable to mouse image geometry and
437 scaling. Further details can be found in the various documentation sources for these ANTsX
438 packages.

439 4.1.3 Template generation

440 ANTsX provides functionality for constructing templates from a set (or multi-modal sets) of
441 input images as originally described⁴⁵ and recently used to create the DevCCF templates.¹⁵
442 An initial template estimate is constructed from an existing subject image or a voxelwise
443 average derived from a rigid pre-alignment of the image population. Pairwise registration
444 between each subject and the current template estimate is performed using the Symmetric
445 Normalization (SyN) algorithm.⁴¹ The template estimate is updated by warping all subjects
446 to the space of the template, performing a voxelwise average, and then performing a “shape
447 update” of this latter image by warping it by the average inverse deformation, thus yielding
448 a mean image of the population in terms of both intensity and shape. The corresponding

449 ANTsPy function is `ants.build_template(...)`.

450 4.1.4 Visualization

451 To complement the well-known visualization capabilities of R and Python, e.g., `ggplot2`
452 and `matplotlib`, respectively, image-specific visualization capabilities are available in the
453 `ants.plot(...)` function (Python). These are capable of illustrating multiple slices in
454 different orientations with other image overlays and label images.

455 4.2 Mapping fMOST data to AllenCCFv3

456 4.2.1 Preprocessing

- 457 • *Downsampling.* The first challenge when mapping fMOST images into the AllenCCFv3
458 is addressing the resolution scale of the data. Native fMOST data from an individual
459 specimen can range in the order of terabytes, which leads to two main problems. First,
460 volumetric registration methods (particularly those estimating local deformation) have
461 high computational complexity and typically cannot operate on such high-resolution
462 data under reasonable memory and runtime constraints. Second, the resolution of
463 the AllenCCFv3 atlas is much lower than the fMOST data, thus the mapping process
464 will cause much of the high-resolution information in the fMOST images to be lost
465 regardless. Thus, we perform a cubic B-spline downsampling of the fMOST data to
466 reduce the resolution of each image to match the isotropic $25 \mu\text{m}$ voxel resolution of the
467 AllenCCFv3 intensity atlas using `ants.resample_image(...)`. An important detail
468 to note is that while the fMOST images and atlas are downsampled, the mapping
469 learned during the registration is assumed to be continuous. Thus, after establishing
470 the mapping to the AllenCCFv3, we can interpolate the learned mapping and apply it
471 directly to the high-resolution native data directly to transform any spatially aligned
472 data (such as the single-cell neuron reconstructions) into the AllenCCFv3.

- 473 • *Stripe artifact removal.* Repetitive pattern artifacts are a common challenge in fMOST
474 imaging where inhomogeneity during the cutting and imaging of different sections can

475 leave stripes of hyper- and hypo-intensity across the image. These stripe artifacts
476 can be latched onto by the registration algorithm as unintended features that are
477 then misregistered to non-analogous structures in the AllenCCFv3. We address these
478 artifacts by fitting a 3-D bandstop (notch) filter to target the frequency of the stripe
479 patterns and removing them prior to the image registration.

- 480 • *Inhomogeneity correction.* Regional intensity inhomogeneity can also occur within
481 and between sections in fMOST imaging due to staining or lighting irregularity during
482 acquisition. Similar to stripe artifacts, intensity gradients due to inhomogeneity
483 can be misconstrued as features during the mapping and result in matching of non-
484 corresponding structures. Our pipeline addresses these intensity inhomogeneities using
485 N4 bias field correction,²⁵ `ants.n4_bias_field_correction(...)`.

486 **4.2.2 Steps for spatial normalization to AllenCCFv3**

- 487 1. *Average fMOST atlas as an intermediate target.* Due to the preparation of the mouse
488 brain for fMOST imaging, the resulting structure in the mouse brain has several large
489 morphological deviations from the AllenCCFv3 atlas. Most notable of these is an en-
490 largement of the ventricles, and compression of cortical structures. In addition, there is
491 poor intensity correspondence for the same anatomic features due to intensity dissim-
492 ilarity between imaging modalities. We have found that standard intensity-base reg-
493 istration is insufficient to capture the significant deformations required to map these
494 structures correctly into the AllenCCFv3. We address this challenge in ANTsX by
495 using explicitly corresponding parcellations of the brain, ventricles and surrounding
496 structures to directly recover these large morphological differences. However, generat-
497 ing these parcellations for each individual mouse brain is a labor-intensive task. Our
498 solution is to create an average atlas whose mapping to AllenCCFv3 encapsulates these
499 large morphological differences to serve as an intermediate registration point. This has
500 the advantage of only needing to generate one set of corresponding annotations which
501 is used to register between the two atlas spaces. New images are first aligned to the
502 fMOST average atlas, which shares common intensity and morphological features and

503 thus can be achieved through standard intensity-based registration.

- 504 2. *Average fMOST atlas construction.* An intensity and shape-based contralaterally sym-
505 metric average of the fMOST image data is constructed from 30 images and their
506 contralateral flipped versions. We ran three iterations of the atlas construction using
507 the default settings. Additional iterations (up to six) were evaluated and showed mini-
508 mal changes to the final atlas construction, suggesting a convergence of the algorithm.
- 509 3. *fMOST atlas to AllenCCFv3 alignment.* Alignment between the fMOST average atlas
510 and AllenCCFv3 was performed using a one-time annotation-driven approach. Label-
511 to-label registration is used to align 7 corresponding annotations in both atlases in
512 the following: 1) brain mask/ventricles, 2) caudate/putamen, 3) fimbria, 4) posterior
513 choroid plexus, 5) optic chiasm, 6) anterior choroid plexus, and 7) habenular com-
514 missure. The alignments were performed sequentially, with the largest, most relevant
515 structures being aligned first using coarse registration parameters, followed by other
516 structures using finer parameters. This coarse-to-fine approach allows us to address
517 large morphological differences (such as brain shape and ventricle expansion) at the
518 start of registration and then progressively refine the mapping using the smaller struc-
519 tures. The overall ordering of these structures was determined manually by an expert
520 anatomist, where anatomical misregistration after each step of the registration was
521 evaluated and used to determine which structure should be used in the subsequent it-
522 eration to best improve the alignment. The transformation from this one-time expert-
523 guided alignment is preserved and used as the canonical fMOST atlas to AllenCCFv3
524 mapping in the pipeline.
- 525 4. *Alignment of individual fMOST mouse brains.* The canonical transformation between
526 the fMOST atlas and AllenCCFv3 greatly simplifies the registration of new individ-
527 ual fMOST mouse brains into the AllenCCFv3. Each new image is first registered
528 into the fMOST average atlas, which shares intensity, modality, and morpholog-
529 ical characteristics. This allows us to leverage standard, intensity-based registration
530 functionality⁶⁸ available in ANTsX to perform this alignment. Transformations are
531 then concatenated to the original fMOST image to move it into the AllenCCFv3 space

532 using ants.apply_transforms(...).

533 5. *Transformation of single cell neurons.* A key feature of fMOST imaging is the ability
534 to reconstruct and examine whole-brain single neuron projections⁶³. Spatial mapping
535 of these neurons from individual brains into the AllenCCFv3 allows investigators to
536 study different neuron types within the same space and characterize their morphology
537 with respect to their transcriptomics. Mappings found between the fMOST image
538 and the AllenCCFv3 using our pipeline can be applied in this way to fMOST neuron
539 reconstruction data.

540 **4.3 Mapping MERFISH data to AllenCCFv3**

541 **4.3.1 Preprocessing**

- 542 • *Initial volume reconstruction.* Alignment of MERFISH data into a 3-D atlas space
543 requires an estimation of anatomical structure within the data. For each section,
544 this anatomic reference image was created by aggregating the number of detected
545 genetic markers (across all probes) within each pixel of a $10 \times 10\mu m^2$ grid to match
546 the resolution of the $10\mu m$ AllenCCFv3 atlas. These reference image sections are then
547 coarsely reoriented and aligned across sections using manual annotations of the most
548 dorsal and ventral points of the midline. The procedure produces an anatomic image
549 stack that serves as an initialization for further global mappings into the AllenCCFv3.
- 550 • *Anatomical correspondence labeling.* Mapping the MERFISH data into the AllenCCFv3
551 requires us to establish correspondence between the anatomy depicted in the MERFISH
552 and AllenCCFv3 data. Intensity-based features in MERFISH data are not sufficiently
553 apparent to establish this correspondence, so we need to generate instead corresponding
554 anatomical labelings of both images with which to drive registration. These labels are
555 already available as part of the AllenCCFv3; thus, the main challenge is deriving
556 analogous labels from the spatial transcriptomic maps of the MERFISH data. Toward
557 this end, we assigned each cell from the scRNA-seq dataset to one of the following
558 major regions: cerebellum, CTXsp, hindbrain, HPF, hypothalamus, isocortex, LSX,

midbrain, OLF, PAL, sAMY, STRd, STRv, thalamus and hindbrain. A label map of each section was generated for each region by aggregating the cells assigned to that region within a $10 \times 10\mu\text{m}^2$ grid. The same approach was used to generate more fine grained region specific landmarks (i.e., cortical layers, habenula, IC). Unlike the broad labels which cover large swaths of the section these regions are highly specific to certain parts of the section. Once cells in the MERFISH data are labeled, morphological dilation is used to provide full regional labels for alignment into the AllenCCFv3.

- *Section matching.* Since the MERFISH data is acquired as sections, its 3-D orientation may not be fully accounted for during the volume reconstruction step, due to the particular cutting angle. This can lead to obliqueness artifacts in the section where certain structures can appear to be larger or smaller, or missing outright from the section. To address this, we first use a global alignment to match the orientations of the MERFISH sections to the atlas space. In our pipeline, this section matching is performed in the reverse direction by performing a global affine transformation of the AllenCCFv3 into the MERFISH data space, and then resampling digital sections from the AllenCCFv3 to match each MERFISH section. This approach limits the overall transformation and thus resampling that is applied to the MERFISH data, and, since the AllenCCFv3 is densely sampled, it also reduces in-plane artifacts that result from missing sections or undefined spacing in the MERFISH data.

4.3.2 2.5D deformable, landmark-driven alignment to AllenCCFv3

After global alignment of the AllenCCFv3 into the MERFISH dataset, 2D per-section deformable refinements are used to address local differences between the MERFISH sections and the resampled AllenCCFv3 sections. Nine registrations were performed in sequence using a single label at each iteration in the following order: 1) brain mask, 2) isocortex (layer 2+3), 3) isocortex (layer 5), 4) isocortex (layer 6), 5) striatum, 6) medial habenula, 7) lateral habenula, 8) thalamus, and 9) hippocampus. This ordering was determined empirically by an expert anatomist who prioritized which structure to use in each iteration by evaluating the anatomical alignment from the previous iteration. Global and local mappings are

587 then all concatenated (with appropriate inversions) to create the final mapping between the
588 MERFISH data and AllenCCFv3. This mapping is then used to provide a point-to-point
589 correspondence between the original MERFISH coordinate space and the AllenCCFv3 space,
590 thus allowing mapping of individual genes and cell types located in the MERFISH data to
591 be directly mapped into the AllenCCFv3.

592 4.4 DevCCF velocity flow transformation model

593 Given multiple, linearly or non-linearly ordered point sets where individual points across the
594 sets are in one-to-one correspondence, we developed an approach for generating a velocity
595 flow transformation model to describe a time-varying diffeomorphic mapping as a variant of
596 the landmark matching solution. Integration of the resulting velocity field can then be used
597 to describe the displacement between any two time points within this time-parameterized
598 domain. Regularization of the sparse correspondence between point sets is performed using
599 a generalized B-spline scattered data approximation technique,⁶⁷ also created by the ANTsX
600 developers and contributed to ITK.

601 4.4.1 Velocity field optimization

602 To apply this methodology to the developmental templates,¹⁵ we coalesced the manual an-
603 notations of the developmental templates into 26 common anatomical regions (see Figure 3).
604 We then used these regions to generate invertible transformations between successive time
605 points. Specifically each label was used to create a pair of single region images resulting in 26
606 pairs of “source” and “target” images. The multiple image pairs were simultaneously used to
607 iteratively estimate a diffeomorphic pairwise transform. Given the seven atlases E11.5, E13.5,
608 E15.5, E18.5, P4, P14, and P56, this resulted in 6 sets of transforms between successive time
609 points. Approximately 10^6 points were randomly sampled labelwise in the P56 template
610 space and propagated to each successive atlas providing the point sets for constructing the
611 velocity flow model. Approximately 125 iterations resulted in a steady convergence based
612 on the average Euclidean norm between transformed point sets. Ten integration points were

613 used and point sets were distributed along the temporal dimension using a log transform for
614 a more evenly spaced sampling. For additional information a help menu is available for the
615 ANTsPy function `ants.fit_time_varying_transform_to_point_sets(...)`.

616 4.5 ANTsXNet mouse brain applications

617 4.5.1 General notes regarding deep learning training

618 All network-based approaches described below were implemented and organized in the
619 ANTsXNet libraries comprising Python (ANTsPyNet) and R (ANTsRNet) analogs using
620 the Keras/Tensorflow libraries available as open-source in ANTsX GitHub repositories.
621 For the various applications, both share the identically trained weights for mutual re-
622 producibility. For all GPU training, we used Python scripts for creating custom batch
623 generators which we maintain in a separate GitHub repository for public availability
624 (<https://github.com/ntustison/ANTsXNetTraining>). These scripts provide details such as
625 batch size, choice of loss function, and network parameters. In terms of GPU hardware, all
626 training was done on a DGX (GPUs: 4X Tesla V100, system memory: 256 GB LRDIMM
627 DDR4).

628 Data augmentation is crucial for generalizability and accuracy of the trained networks.
629 Intensity-based data augmentation consisted of randomly added noise (i.e., Gaussian, shot,
630 salt-and-pepper), simulated bias fields based on N4 bias field modeling, and histogram warp-
631 ing for mimicking well-known MRI intensity nonlinearities.^{26,70} These augmentation tech-
632 niques are available in ANTsXNet (only ANTsPyNet versions are listed with ANTsRNet
633 versions available) and include:

- 634 • image noise: `ants.add_noise_to_image(...)`,
- 635 • simulated bias field: `antspynet.simulate_bias_field(...)`, and
- 636 • nonlinear intensity warping: `antspynet.histogram_warp_image_intensities(...)`.

637 Shape-based data augmentation used both random linear and nonlinear deformations in
638 addition to anisotropic resampling in the three canonical orientations to mimic frequently
639 used acquisition protocols for mice brains:

- 640 • random spatial warping: `antspynet.randomly_transform_image_data(...)` and
641 • anisotropic resampling: `ants.resample_image(...)`.

642 **4.5.2 Brain extraction**

643 Similar to human neuroimage processing, brain extraction is a crucial preprocessing step
644 for accurate brain mapping. We developed similar functionality for T2-weighted mouse
645 brains. This network uses a conventional U-net architecture⁷¹ and, in ANTsPyNet, this
646 functionality is available in the program `antspynet.mouse_brain_extraction(...)`.
647 For the two-shot T2-weighted brain extraction network, two brain templates were gen-
648 erated along with their masks. One of the templates was generated from orthogonal
649 multi-plane, high resolution data⁵⁸ which were combined to synthesize isotropic volu-
650 metric data using the B-spline fitting algorithm.⁶⁷ This algorithm is encapsulated in
651 `ants.fit_bspline_object_to_scattered_data(...)` where the input is the set of voxel
652 intensity values and each associated physical location. Since each point can be assigned
653 a confidence weight, we use the normalized gradient value to more heavily weight edge
654 regions. Although both template/mask pairs are available in the GitHub repository
655 associated with this work, the synthesized volumetric B-spline T2-weighted pair is available
656 within ANTsXNet through the calls:

- 657 • template: `antspynet.get_antsxnet_data("bsplineT2MouseTemplate")` and
658 • mask: `antspynet.get_antsxnet_data("bsplineT2MouseTemplateBrainMask")`.

659 **4.5.3 Brain parcellation**

660 The T2-weighted brain parcellation network is also based on a 3-D U-net architecture and the
661 T2-w DevCCF P56 template component with extensive data augmentation, as described pre-

662 viously. Intensity differences between the template and any brain extracted input image are
663 minimized through the use of the rank intensity transform (`ants.rank_intensity(...)`).
664 Shape differences are reduced by the additional preprocessing step of warping the brain ex-
665 tracted input image to the template. Additional input channels include the prior probability
666 images created from the template parcellation. These images are also available through the
667 ANTsXNet `get_antsxnet_data(...)` interface.

668 **Data availability.** All data and software used in this work are publicly available. The
669 DevCCF atlas is available at <https://kimlab.io/brain-map/DevCCF/>. ANTsPy, ANTsR,
670 ANTsPyNet, and ANTsRNet are available through GitHub at the ANTsX Ecosystem (<https://github.com/ANTsX>). Training scripts for all deep learning functionality in ANTsXNet can
671 also be found on GitHub (<https://github.com/ntustison/ANTsXNetTraining>). A GitHub
672 repository specifically pertaining to the AllenCCFv3 mapping is available at <https://github.com/dontminchenit/CCFAlignmentToolkit>. For the other two contributions contained in
673 this work, the longitudinal DevCCF mapping and mouse cortical thickness pipeline, we refer
674 the interested reader to <https://github.com/ntustison/ANTsXMouseBrainMapping>.

677 **References**

- 678 1. Keller, P. J. & Ahrens, M. B. Visualizing whole-brain activity and development at
679 the single-cell level using light-sheet microscopy. *Neuron* **85**, 462–83 (2015).
- 680 2. La Manno, G. *et al.* Molecular architecture of the developing mouse brain. *Nature*
681 **596**, 92–96 (2021).
- 682 3. Wen, L. *et al.* Single-cell technologies: From research to application. *Innovation*
683 (*Camb*) **3**, 100342 (2022).
- 684 4. Oh, S. W. *et al.* A mesoscale connectome of the mouse brain. *Nature* **508**, 207–14
685 (2014).
- 686 5. Gong, H. *et al.* Continuously tracing brain-wide long-distance axonal projections in
687 mice at a one-micron voxel resolution. *Neuroimage* **74**, 87–98 (2013).
- 688 6. Li, A. *et al.* Micro-optical sectioning tomography to obtain a high-resolution atlas of
689 the mouse brain. *Science* **330**, 1404–8 (2010).
- 690 7. Ueda, H. R. *et al.* Tissue clearing and its applications in neuroscience. *Nat Rev*
691 *Neurosci* **21**, 61–79 (2020).
- 692 8. Ståhl, P. L. *et al.* Visualization and analysis of gene expression in tissue sections by
693 spatial transcriptomics. *Science* **353**, 78–82 (2016).
- 694 9. Burgess, D. J. Spatial transcriptomics coming of age. *Nat Rev Genet* **20**, 317 (2019).
695
- 696 10. MacKenzie-Graham, A. *et al.* A multimodal, multidimensional atlas of the C57BL/6J
697 mouse brain. *J Anat* **204**, 93–102 (2004).
- 698 11. Mackenzie-Graham, A. J. *et al.* Multimodal, multidimensional models of mouse brain.
699 *Epilepsia* **48 Suppl 4**, 75–81 (2007).
- 700 12. Dong, H. W. *Allen reference atlas. A digital color brain atlas of the C57BL/6J male*
701 *mouse.* (John Wiley; Sons, 2008).

- 702 13. Wang, Q. *et al.* The allen mouse brain common coordinate framework: A 3D reference
703 atlas. *Cell* **181**, 936–953.e20 (2020).
- 704 14. Johnson, G. A. *et al.* Waxholm space: An image-based reference for coordinating
705 mouse brain research. *Neuroimage* **53**, 365–72 (2010).
- 706 15. Kronman, F. A. *et al.* Developmental mouse brain common coordinate framework.
707 *bioRxiv* (2023) doi:[10.1101/2023.09.14.557789](https://doi.org/10.1101/2023.09.14.557789).
- 708 16. Oguz, I., Zhang, H., Rumple, A. & Sonka, M. RATS: Rapid automatic tissue segmen-
709 tation in rodent brain MRI. *J Neurosci Methods* **221**, 175–82 (2014).
- 710 17. Sawiak, S. J., Picq, J.-L. & Dhenain, M. Voxel-based morphometry analyses of in
711 vivo MRI in the aging mouse lemur primate. *Front Aging Neurosci* **6**, 82 (2014).
- 712 18. Ashburner, J. SPM: A history. *Neuroimage* **62**, 791–800 (2012).
- 713
- 714 19. Modat, M. *et al.* Fast free-form deformation using graphics processing units. *Comput
715 Methods Programs Biomed* **98**, 278–84 (2010).
- 716 20. Tyson, A. L. *et al.* Accurate determination of marker location within whole-brain
717 microscopy images. *Sci Rep* **12**, 867 (2022).
- 718 21. Pallast, N. *et al.* Processing pipeline for atlas-based imaging data analysis of struc-
719 tural and functional mouse brain MRI (AIDAmri). *Front Neuroinform* **13**, 42 (2019).
- 720 22. Jenkinson, M., Beckmann, C. F., Behrens, T. E. J., Woolrich, M. W. & Smith, S. M.
721 FSL. *Neuroimage* **62**, 782–90 (2012).
- 722 23. Yeh, F.-C., Wedeen, V. J. & Tseng, W.-Y. I. Generalized q-sampling imaging. *IEEE
723 Trans Med Imaging* **29**, 1626–35 (2010).
- 724 24. Jorge Cardoso, M. *et al.* STEPS: Similarity and truth estimation for propagated
725 segmentations and its application to hippocampal segmentation and brain parcelation.
Med Image Anal **17**, 671–84 (2013).

- 726 25. Tustison, N. J. *et al.* N4ITK: Improved N3 bias correction. *IEEE Trans Med Imaging*
727 **29**, 1310–20 (2010).
- 728 26. Tustison, N. J. *et al.* The ANTsX ecosystem for quantitative biological and medical
729 imaging. *Sci Rep* **11**, 9068 (2021).
- 730 27. Goubran, M. *et al.* Multimodal image registration and connectivity analysis for inte-
731 gration of connectomic data from microscopy to MRI. *Nat Commun* **10**, 5504 (2019).
- 732 28. Celestine, M., Nadkarni, N. A., Garin, C. M., Bougacha, S. & Dhenain, M. Sammba-
733 MRI: A library for processing SmAll-MaMmal BrAin MRI data in python. *Front
Neuroinform* **14**, 24 (2020).
- 734 29. Ioanas, H.-I., Marks, M., Zerbi, V., Yanik, M. F. & Rudin, M. An optimized regis-
735 tration workflow and standard geometric space for small animal brain imaging. *Neuro-
image* **241**, 118386 (2021).
- 736 30. Cox, R. W. AFNI: What a long strange trip it's been. *Neuroimage* **62**, 743–7 (2012).
737
- 738 31. Anderson, R. J. *et al.* Small animal multivariate brain analysis (SAMBA) - a high
739 throughput pipeline with a validation framework. *Neuroinformatics* **17**, 451–472
(2019).
- 740 32. Ni, H. *et al.* A robust image registration interface for large volume brain atlas. *Sci
741 Rep* **10**, 2139 (2020).
- 742 33. Jin, M. *et al.* SMART: An open-source extension of WholeBrain for intact mouse
743 brain registration and segmentation. *eNeuro* **9**, (2022).
- 744 34. Fürth, D. *et al.* An interactive framework for whole-brain maps at cellular resolution.
745 *Nat Neurosci* **21**, 139–149 (2018).
- 746 35. Negwer, M. *et al.* FriendlyClearMap: An optimized toolkit for mouse brain mapping
747 and analysis. *Gigascience* **12**, (2022).

- 748 36. Klein, S., Staring, M., Murphy, K., Viergever, M. A. & Pluim, J. P. W. Elastix: A
749 toolbox for intensity-based medical image registration. *IEEE Trans Med Imaging* **29**,
196–205 (2010).
- 750 37. Carey, H. *et al.* DeepSlice: Rapid fully automatic registration of mouse brain imaging
751 to a volumetric atlas. *Nat Commun* **14**, 5884 (2023).
- 752 38. Bajcsy, R. & Broit, C. Matching of deformed images. in *Sixth International Conference
753 on Pattern Recognition (ICPR'82)* 351–353 (1982).
- 754 39. Bajcsy, R. & Kovacic, S. Multiresolution elastic matching. *Computer Vision, Graph-
755 ics, and Image Processing* **46**, 1–21 (1989).
- 756 40. Gee, J. C., Reivich, M. & Bajcsy, R. Elastically deforming 3D atlas to match anatom-
757 ical brain images. *J Comput Assist Tomogr* **17**, 225–36 (1993).
- 758 41. Avants, B. B., Epstein, C. L., Grossman, M. & Gee, J. C. Symmetric diffeomorphic
759 image registration with cross-correlation: Evaluating automated labeling of elderly
and neurodegenerative brain. *Med Image Anal* **12**, 26–41 (2008).
- 760 42. Klein, A. *et al.* Evaluation of 14 nonlinear deformation algorithms applied to human
761 brain MRI registration. *Neuroimage* **46**, 786–802 (2009).
- 762 43. Murphy, K. *et al.* Evaluation of registration methods on thoracic CT: The EMPIRE10
763 challenge. *IEEE Trans Med Imaging* **30**, 1901–20 (2011).
- 764 44. Baheti, B. *et al.* The brain tumor sequence registration challenge: Establishing corre-
765 spondence between pre-operative and follow-up MRI scans of diffuse glioma patients.
(2021).
- 766 45. Avants, B. B. *et al.* The optimal template effect in hippocampus studies of diseased
767 populations. *Neuroimage* **49**, 2457–66 (2010).
- 768 46. Avants, B. B., Tustison, N. J., Wu, J., Cook, P. A. & Gee, J. C. An open source
769 multivariate framework for n-tissue segmentation with evaluation on public data.
Neuroinformatics **9**, 381–400 (2011).

- 770 47. Manjón, J. V., Coupé, P., Martí-Bonmatí, L., Collins, D. L. & Robles, M. Adaptive
771 non-local means denoising of MR images with spatially varying noise levels. *J Magn*
Reson Imaging **31**, 192–203 (2010).
- 772 48. Wang, H. *et al.* Multi-atlas segmentation with joint label fusion. *IEEE Trans Pattern*
773 *Anal Mach Intell* **35**, 611–23 (2013).
- 774 49. Tustison, N. J. *et al.* Optimal symmetric multimodal templates and concatenated
775 random forests for supervised brain tumor segmentation (simplified) with ANTsR.
Neuroinformatics (2014) doi:[10.1007/s12021-014-9245-2](https://doi.org/10.1007/s12021-014-9245-2).
- 776 50. Tustison, N. J., Yang, Y. & Salerno, M. Advanced normalization tools for cardiac mo-
777 tion correction. in *Statistical atlases and computational models of the heart - imaging*
and modelling challenges (eds. Camara, O. *et al.*) vol. 8896 3–12 (Springer Interna-
778 tional Publishing, 2015).
- 779 51. McCormick, M., Liu, X., Jomier, J., Marion, C. & Ibanez, L. ITK: Enabling repro-
780 ducible research and open science. *Front Neuroinform* **8**, 13 (2014).
- 781 52. Beg, M. F., Miller, M. I., Trouvé, A. & Younes, L. Computing large deformation
782 metric mappings via geodesic flows of diffeomorphisms. *International Journal of*
Computer Vision **61**, 139–157 (2005).
- 783 53. Tustison, N. J. & Avants, B. B. Explicit B-spline regularization in diffeomorphic image
784 registration. *Front Neuroinform* **7**, 39 (2013).
- 785 54. Das, S. R., Avants, B. B., Grossman, M. & Gee, J. C. Registration based cortical
786 thickness measurement. *Neuroimage* **45**, 867–79 (2009).
- 787 55. Tustison, N. J. *et al.* Large-scale evaluation of ANTs and FreeSurfer cortical thickness
788 measurements. *Neuroimage* **99**, 166–79 (2014).
- 789 56. Tustison, N. J. *et al.* Longitudinal mapping of cortical thickness measurements: An
Alzheimer’s Disease Neuroimaging Initiative-based evaluation study. *J Alzheimers*
Dis (2019) doi:[10.3233/JAD-190283](https://doi.org/10.3233/JAD-190283).

- 790 57. Hsu, L.-M. *et al.* CAMRI mouse brain MRI data.
- 791
- 792 58. Reshetnikov, V. *et al.* High-resolution MRI data of brain C57BL/6 and BTBR mice
793 in three different anatomical views.
- 794 59. Rahman, N., Xu, K., Budde, M. D., Brown, A. & Baron, C. A. A longitudinal
795 microstructural MRI dataset in healthy C57Bl/6 mice at 9.4 tesla. *Sci Data* **10**, 94
795 (2023).
- 796 60. Gong, H. *et al.* High-throughput dual-colour precision imaging for brain-wide connec-
797 tome with cytoarchitectonic landmarks at the cellular level. *Nat Commun* **7**, 12142
797 (2016).
- 798 61. Wang, J. *et al.* Divergent projection patterns revealed by reconstruction of individual
799 neurons in orbitofrontal cortex. *Neurosci Bull* **37**, 461–477 (2021).
- 800 62. Rotolo, T., Smallwood, P. M., Williams, J. & Nathans, J. Genetically-directed, cell
801 type-specific sparse labeling for the analysis of neuronal morphology. *PLoS One* **3**,
801 e4099 (2008).
- 802 63. Peng, H. *et al.* Morphological diversity of single neurons in molecularly defined cell
803 types. *Nature* **598**, 174–181 (2021).
- 804 64. Yao, Z. *et al.* A high-resolution transcriptomic and spatial atlas of cell types in the
805 whole mouse brain. *Nature* **624**, 317–332 (2023).
- 806 65. Liu, J. *et al.* Concordance of MERFISH spatial transcriptomics with bulk and single-
807 cell RNA sequencing. *Life Sci Alliance* **6**, (2023).
- 808 66. Stringer, C., Wang, T., Michaelos, M. & Pachitariu, M. Cellpose: A generalist algo-
809 rithm for cellular segmentation. *Nat Methods* **18**, 100–106 (2021).
- 810 67. Tustison, N. J. & Amini, A. A. Biventricular myocardial strains via nonrigid regis-
811 tration of anatomical NURBS model [corrected]. *IEEE Trans Med Imaging* **25**, 94–112
(2006).

- 812 68. Avants, B. B. *et al.* The Insight ToolKit image registration framework. *Front Neuroinform* **8**, 44 (2014).
- 813
- 814 69. Avants, B. B. *et al.* A reproducible evaluation of ANTs similarity metric performance
815 in brain image registration. *Neuroimage* **54**, 2033–44 (2011).
- 816 70. Nyúl, L. G., Udupa, J. K. & Zhang, X. New variants of a method of MRI scale
817 standardization. *IEEE Trans Med Imaging* **19**, 143–50 (2000).
- 818 71. Falk, T. *et al.* U-net: Deep learning for cell counting, detection, and morphometry.
819 *Nat Methods* **16**, 67–70 (2019).